



Influence of the shape of Ni catalysts in the glycerol steam reforming

L.F. Bobadilla^{a,*}, A. Álvarez^a, M.I. Domínguez^a, F. Romero-Sarria^a, M.A. Centeno^a,
M. Montes^b, J.A. Odriozola^a

^a Departamento de Química Inorgánica e Instituto de Ciencia de Materiales, Centro mixto Universidad de Sevilla-CSIC, Av. Américo Vespucio, 41092 Sevilla, Spain

^b Grupo de Ingeniería Química, Departamento de Química Aplicada, Facultad de Ciencias Químicas, UPV/EHU, Paseo Manuel de Lardizábal, 3, 20018 San Sebastián, Spain

ARTICLE INFO

Article history:

Received 29 February 2012

Received in revised form 27 April 2012

Accepted 2 May 2012

Available online 9 May 2012

Keywords:

Monoliths

Conventional catalyst

Glycerol steam reforming

Coke

ABSTRACT

Biomass is an alternative to replace the use of fossil fuels. Glycerol, a byproduct in the biodiesel production, can be used for obtaining hydrogen. The most efficient method for obtaining hydrogen from glycerol is the steam reforming (SR). So far all the published papers report the use of conventional catalyst. In this paper, a structured catalyst has been prepared and compared with the conventional ones (powder and spherical pellets). Results show that the structured catalyst (monolith) is more stable as formation of coke was not observed.

© 2012 Elsevier B.V. All rights reserved.

1. Introduction

The increasing energy demand and the global warming problem owed to the use of fossil fuels indicate a need to find petroleum alternatives to satisfy our fuel needs. Proton exchange membrane fuel cells (PEMFC), an attractive alternative for powering electric vehicles and electronic portable equipment [1], requires the use of almost pure hydrogen.

The process and technology for hydrogen production have been changing in the past few years. Most hydrogen is produced from natural gas and oil fractions, which are still the most abundant and economically feasible raw materials. However, natural gas and oil are fossil fuels and their use produce high quantities of carbon dioxide during reforming [2].

The development of hydrogen production systems from renewable sources may help in reducing the impact of greenhouse gas (GHG) emissions. This has resulted in a great effort for developing hydrogen production systems by reforming renewable sources, and in particular, hydrogen-containing by-products of industrial or domestic wastes [3–9]. Within this waste-to-energy approach, glycerol is a potential candidate for hydrogen production. In converting triglycerides into biodiesel approximately 10 wt% glycerol is produced as byproduct. The increased biodiesel production

will result in an overabundance of glycerol flooding the market, reducing the price of this valuable product, converting it in a waste and, therefore, compromising the economic feasibility of biodiesel production from renewable triglycerides. Hydrogen production merges as a feasible option for glycerol valorization, in particular, if produced in situ through reforming using microchannel technologies [10].

Literature data show that transition metal catalysts active in the steam reforming of methanol (SRM) reaction are also active for the steam reforming of glycerol (SRG), among them nickel has been used [11]. Nevertheless, the main drawback of using nickel catalysts is the high carbon formation rate [12]. In their study of the aqueous phase reforming of glycerol, Cortright et al. [13] proposed that by adding Sn to the Ni catalyst the selectivity for hydrogen production increases while the selectivity toward alkanes, the coke precursors, decreases. Trimm [14] hypothesized that the similar electronic structure of carbon and elements of groups IV and V of the periodic table may favor the interaction of these metals with Ni 3d electrons, thereby reducing the chance of nickel carbide formation. Shabaker et al. [15] proposed a model for Ni-Sn/Al₂O₃ catalyst particles consisting of a Ni₃Sn phase around a core of Ni, obtaining indirect evidence for the alloy formation. A direct evidence for the formation of the Ni-Sn has been obtained using XRD on NiSn/MgO-Al₂O₃ catalysts [16]. More recently, Bobadilla et al. [17] have shown that alloying tin with nickel results in a complex mixture of phases whose proportion is determined by the preparation method and the Ni-Sn thermodynamics (phase diagram), the dominant phase being Ni₃Sn₂. Alternatively, gasifying the deposited carbon species may reduce coking [18–20]. The modification of

* Corresponding author at: Laboratoire Catalyse et Spectrochimie, UMR 6506, ENSICAen 6, bd Maréchal Juin, 14050 Caen Cedex, France. Tel.: +33 231 451 348; fax: +33 231 452 822.

E-mail address: luis.bobadilla@ensicaen.fr (L.F. Bobadilla).

the supports by adding alkaline components such as MgO, K₂O or lanthanide oxides [16,21–24] favors coke gasification. Therefore, the combination of basic promoters and a group IV alloying element result in favoring coke-resistant Ni catalysts for the SR of hydrocarbons.

Coke formation is observed for the pyrolysis and the steam gasification of glycerol in the absence of catalysts [25–29]. Moreover, the SR of glycerol results in coke formation for most catalysts and temperatures investigated [11,28–32]. However, thermodynamic studies have shown that for the steam-to-carbon ratio used in this work the thermodynamic coking limit of our system is well below 4 in all the temperature range used, since high temperature promotes the oxidation, gasification, and reforming of carbon [31]. For instance, coke will be eliminated, from a thermodynamic point of view, above 563 °C and steam-to-carbon ratios above 1 in the glycerol reforming, although its gasification may be kinetically slow [33] requiring a careful tailoring of the operational conditions since, in general, the carbon deposition rate is faster than the carbon removal rate, which results in exponential-like deposition behavior [28]. Thus, low amounts of deposited coke are observed for the SR of glycerol over Ni-ZrO₂/CeO₂ catalysts in the temperature range 600–700 °C using 10 and 20 wt% glycerol feed solutions [32]. Although these authors assumed that the low amount of coke formed is probably due to the CeO₂ capacity to store and transfer oxygen and as a result to promote the gasification of the carbonaceous specie deposited, Araque et al. show that ceria–zirconia supported Co or Co–Rh bimetallic active phases deactivate in the SR of glycerol by formation of carbonaceous deposits [30], the main difference being the increased relative amount of glycerol in the feed stream as high as 35 wt%. Moreover, although using similar temperatures and steam-to-carbon ratios in the glycerol SR over Ru/Y₂O₃ catalysts Hirai et al. [11] report the absence of carbon deposits it must be noticed that the glycerol–water mixture feed to the reactor was sweep with Ar resulting in very low glycerol molar flows in the reaction stream.

Conventional packed-bed reactors have been mostly used for the glycerol SR. In these systems, the use of small catalyst particles or *egg-shell* pellets with thin catalytic layers reduces the internal mass-transfer limitations although they are also limited by relatively high pressure drops, flow maldistribution and eventually hot spots that alter the selectivity of the process. Structured catalysts overcome these drawbacks. The employ of metallic monolithic catalysts allows the use of very small parallel channels, well below 1 mm, resulting in process intensification on favoring heat and mass transfer during reaction. In addition to this, metallic monoliths are excellent models for the initial studies of microchannel reactors in which coupled endo- and exothermic reactions are used for controlling the process selectivity [34,35].

In this work, we compare the catalytic activity and selectivity to hydrogen for glycerol SR using diluted powders, *egg-shell* pellets and monolithic catalysts. For performing this comparison we have chosen a NiSn catalyst (Ni-to-Sn atomic ratio equal to 6) supported on a 10 wt% MgO and 15 wt% CeO₂ modified alumina support previously used by us in the SR of methanol [16].

2. Materials and methods

2.1. Preparation of conventional catalysts (powder and pellets)

NiSn powder catalysts were prepared by impregnation. The alumina support was obtained by ball milling 20 g γ -Al₂O₃ (Spherulite SCS505) in 10 mL of ethanol using a PM4, Retsch instrument. A unimodal particle size distribution centered at 7–8 μ m was obtained after 2 h at 300 rpm. Once milled, the alumina support was modified with 10 wt% MgO and 15 wt% CeO₂. Aqueous

Table 1

Chemical composition of powder and pellets catalysts.

wt%	Al	Ce	Mg	Ni	Sn
Powder	43	17	10	25	5
Pellets	46	16	12	20	6

solutions of magnesium nitrate hexahydrate (Mg(NO₃)₂·6H₂O, Aldrich) and cerium nitrate hexahydrate (Ce(NO₃)₃·6H₂O, Fluka) were impregnated onto the alumina powders by the incipient wetness technique, followed by drying overnight at 120 °C in an oven. The resulting solid was further impregnated with an aqueous solution of nickel (II) nitrate hexahydrate (Ni(NO₃)₂·6H₂O, Panreac) and anhydrous tin (II) chloride (SnCl₂, Fluka) in order to obtain a final 26 wt% metallic content and a Ni-to-Sn atomic ratio equal to 6. After impregnation, the catalyst was dried at 120 °C overnight and finally calcined in air at 700 °C for 12 h. The *egg-shell* pellets were prepared similarly but impregnating the aqueous solution onto the alumina spheres. Nevertheless, to avoid the spheres to break during the preparation process, the precursor salts were dissolved in ethanol and the solutions and the alumina spheres submitted to a rotavapor for removing the excess solvent. In Table 1 are included the chemical composition measured by XRF analysis in both catalysts.

2.2. Preparation of the monolithic catalyst

Cylindrical monoliths were prepared using 50 μ m thick AluChrom YHF[®] foils by rolling around a spindle alternate flat and corrugated foils ($L=30$ mm, $d=16$ mm, $V=6$ cm³, cell density 1100 cells/in.²). Washcoating was selected for coating the microchannels with the NiSn catalyst. Prior to washcoat, the metallic monoliths were calcined in air at 900 °C for 22 h in order to generate an adherent α -Al₂O₃ scale [36]. The first step for washcoating a metallic substrate is to prepare stable slurries of the catalyst to be deposited [36–39]. Particle size, solid content of the suspension and pH of the catalyst slurry are parameters that influence the slurry stability. The average particle size of our catalyst after milling in an agate mortar, $D(4,3)=12.7$ μ m, is close to the upper recommend limit for preparing stable slurries [40]. The isoelectric point (IEP) of the catalyst is 7.8 and therefore the pH was fixed at 3.5 using acetic acid for ensuring high values of zeta potential and then high repulsions between the particles, favoring the stability of the slurries [41]. The use of additives for the slurry formulation attempts to improve the catalyst adherence and the washcoating drying process. The addition of colloidal alumina (Nyacol, 20 wt% Al₂O₃), that presents a narrow particle size distribution, improves the catalyst adherence [40,42] according to the model previously proposed by Nijhuis et al. [43] a bimodal particle size distribution increase adherence since the smaller particles are located between the bigger ones. After several trials of slurry formulation for washcoating the following proportions of catalyst and colloidal alumina was selected: 61 wt% catalyst content and 39 wt% colloidal alumina, being the total solid content of the suspension of ca. 24 wt%. The structured supports were dipped into the slurry for 60 s, withdrawn at constant speed and then the excess suspension eliminated by centrifugation at 500 rpm for 5 min. This procedure was repeated several times with intermediate drying steps at 120 °C for 30 min between coatings until ca. 200 mg of the catalysts were deposited. Finally, the coated structured supports were calcined at 700 °C for 12 h. This procedure resulted in a monolith loading of 0.56 mg cm^{−2} catalyst after four washcoating processes. The adherence of the resulting catalytic layer measured with the ultrasound test [44] is better than 97%.

2.3. Characterization

X-ray diffraction (XRD) analysis was carried out on a PANalytical X'PERT PRO diffractometer. Diffraction patterns were recorded using Cu K α radiation ($\lambda = 1.5404 \text{ \AA}$) over a 2θ range using a position-sensitive detector with 0.05° step size at a scan rate of 1° min^{-1} .

The textural properties were studied by N_2 adsorption–desorption isotherms at liquid nitrogen temperature in a Micromeritics ASAP 2020 apparatus between 0.1 and 0.995 relative pressure using, for the monolith, a homemade cell that allows analyzing the complete monolith. Before analysis, the monoliths were degassed for 2 h at 150°C in vacuum. Pore size distribution was calculated using the BJH method.

Scanning electron microscopy (SEM) observations were carried out in a Hitachi S4800 and a Hitachi S2700 instrument equipped with an Energy Dispersive X-ray Spectrometer (Bruker Quantax 400). By SEM were analyzed the cross-sections of the pellets and the monoliths.

Temperature programmed oxidation (TPO) analysis were performed in a U-shaped quartz reactor under oxygen flow (21% in helium) from 25°C to 900°C at a heating rate of $10^\circ\text{C min}^{-1}$. CO_2 evolution was monitored following the $m/z = 44$ signal by mass spectrometry in a Balzers Omnistar Bentchop instrument.

The Raman spectra were recorded using a dispersive Horiba Jobin Yvon LabRaman HR800 Microscope, with a 20 mW He–Ne green laser (532.14 nm) and without filter. The microscope used a $50\times$ objective and a confocal pinhole of $1000 \mu\text{m}$. The Raman spectrometer is calibrated using a silicon wafer.

2.4. Catalytic tests

The glycerol SR was carried out in a computerized commercial Microactivity Reference catalytic reactor (PiD Eng&Tech), employing a Hastelloy C-276 tubular reactor (Autoclave Engineers) with 17 mm internal diameter for the monoliths and 9 mm internal diameter for the powdered and pelletized catalysts. At the reactor outlet a gas–liquid separator was fitted allowing the analysis of

gas and liquid phase products. To avoid flow maldistribution profiles within the reactor, the catalyst powders (100 mg , particle size $\phi = 100\text{--}200 \mu\text{m}$) were diluted with the same amount of crushed quartz sieved to the same particle size range. The exact mass of pellets and monolith catalysts was 150 and 158 mg, respectively. Prior to reaction, the catalyst was reduced at 750°C in 100 mL min^{-1} H_2 (50%, v/v in inert) for 1 h. The experimental runs were conducted at atmospheric pressure with a steam-to-carbon ratio of 4 ($P_{\text{steam}} \approx 90.5 \text{ kPa}$; $P_{\text{gly}} \approx 7.5 \text{ kPa}$) and $100 \text{ L g}^{-1} \text{ h}^{-1}$ space velocity at 750°C . Gas product were analyzed on line using a microGC (Varian 4900) equipped with Porapak Q and MS-5A columns. Liquid products were analyzed by HPLC (Varian 356-LC) equipped with a Refractive Index Detector and a Hi-Plex H column with deionized water as eluent. In Scheme 1 is represented the experimental set-up used in the catalytic tests.

The performance of the catalysts was evaluated in terms of hydrogen yield, Y_H , according to equation:

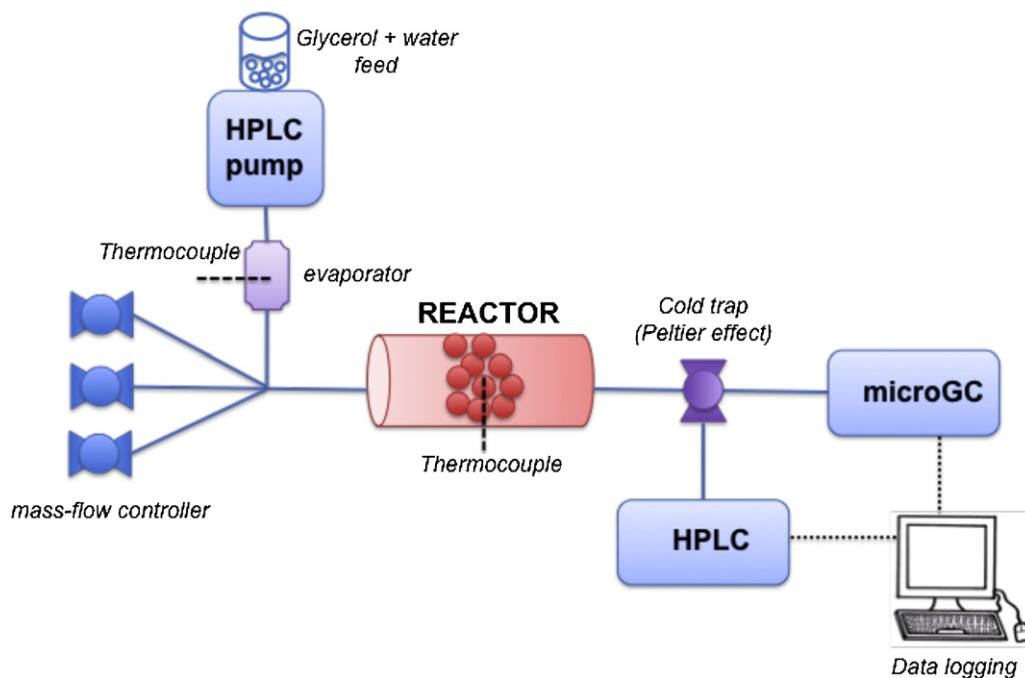
$$Y_H(\%) = \frac{r_H}{7(-r_G)} \times 100$$

where r_H and $(-r_G)$ stand for the formation rate of hydrogen and the glycerol consumption rate to produce gaseous products, respectively.

3. Results and discussion

3.1. Powder and pellets catalysts

Fig. 1 showed the XRD patterns of the prepared catalysts in the form of powder and pellets showing in both cases the presence of MgAl_2O_4 and NiO phases. As previously reported [16], the addition of 10 wt% MgO to the alumina support prevents the formation of nickel spinels improving Ni dispersion. In addition to the diffraction lines corresponding to the above described phases, diffraction peaks at $2\theta = 28.8^\circ$, 33.3° , 47.7° and 56.6° are observed, these are assigned to the (1 1 1), (2 0 0), (2 2 0) and (3 1 1) planes of the cubic structure of cerium oxide. Diffraction peaks associated to Sn and/or NiSn phases were not detected, the low concentration of tin may account for this fact.



Scheme 1. Experimental set-up.

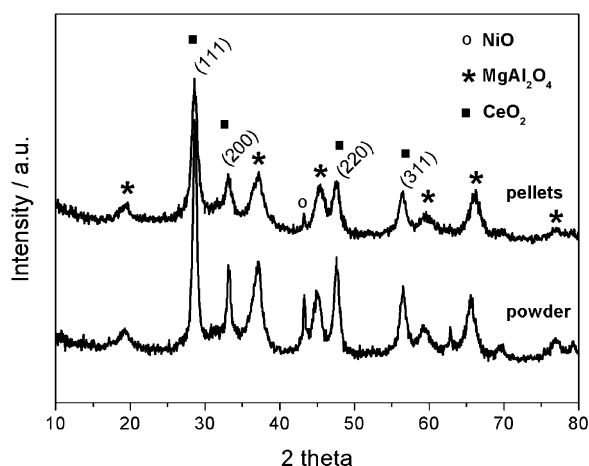


Fig. 1. XRD patterns of powder and pellets catalysts.

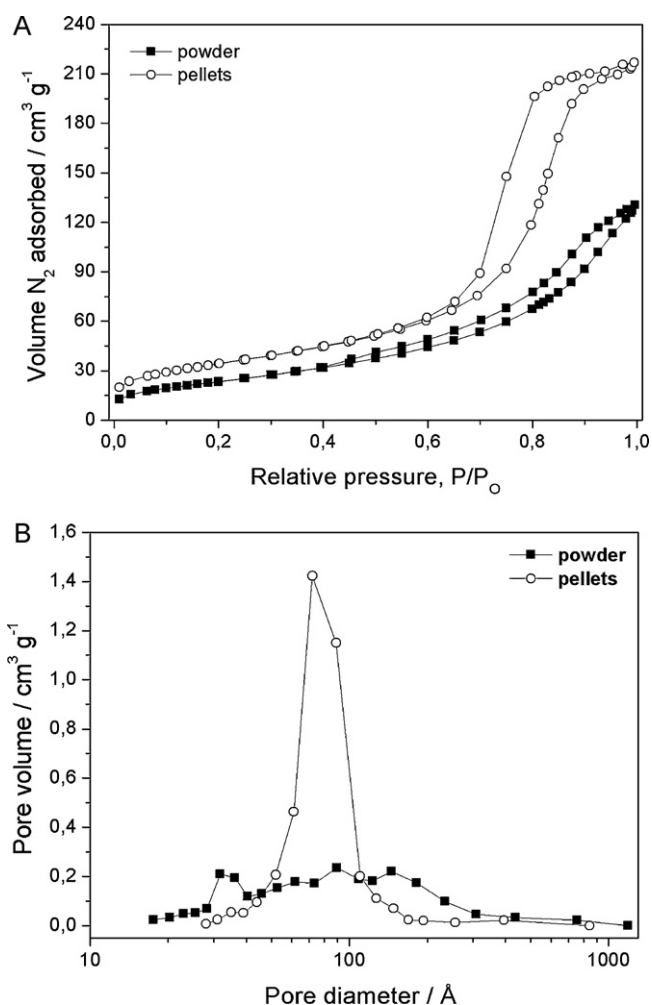


Fig. 2. Adsorption isothermal (A) and pore size distribution (B) for pellets and powder.

Fig. 2A and B shows the adsorption–desorption isotherms and pore size distribution for the catalysts in the form of powder and pellets, respectively. The isotherms are typical of mesoporous materials with complex pores structures. A *H1* hysteresis loop is observed for the catalyst shaped in pellets, which corresponds to the pore system of solids formed by agglomerated spherical particles with uniform pore size. For the catalyst in the form of powder

we observe a *H3* hysteresis loop that must be associated to non-uniform interparticle pores. These isotherms, therefore, results in a monomodal pore size distribution for the pellet catalyst while the powder catalyst present a much broad pore size distribution.

The textural properties of the catalysts and supports are summarized in Table 2. After adding CeO_2 , MgO and Ni-Sn phases the alumina surface area and pore volume considerably decreases, suggesting the incorporation of these phases that do not form solid solution with the alumina into the support pores as early reported [45].

The microstructure of the prepared pellets has been characterized by SEM-EDS of the pellet cross-section, Fig. 3. The microstructure corresponds to a typical *egg-shell* structure formed by an outermost layer containing the Ni-Sn active phase that sits on a MgAl_2O_4 – CeO_2 layer that covers an innermost layer of magnesium–aluminum spinel. The homogeneous elemental distribution of the different elements across the pellet diameter indicates that all these elements have been incorporated through the pore structure of the pellets.

3.2. Structured catalysts

Fig. 4 shows the XRD pattern of the monolithic catalyst together with the diffraction pattern of the preoxidized Aluchrom YHf. The phases present upon high temperature oxidation are the ones expected for an aluminum–alloyed ferritic stainless steel, corundum ($\alpha\text{-Al}_2\text{O}_3$), aluminum yttrium oxide and BCC stainless steel, confirming the formation of an alumina scale on the steel surface that will later help in anchoring the catalyst layer [36]. Upon washcoating, the metallic substrate XRD diffraction lines corresponding to the powder catalyst also appears in the diffraction pattern. The intensity of the diffraction lines corresponding to the metallic substrate and the alumina scale decreases, this indicates a homogeneous deposition of the catalytic layer on top of the alumina scale filling the empty spaces between the alumina needles that form the scale. A detailed description of the anchoring procedure is given elsewhere [36,37,39,40,42,46,47].

Fig. 5A and B shows the adsorption–desorption isotherms and pore size distribution for the monolithic catalyst. This isotherm is typical of mesoporous solids with a *H3* hysteresis loop corresponding to agglomerated particles with a broad pore size distribution. As the surface area of the oxidized metallic monolith is hardly measurable, well below $1\text{ m}^2\text{ g}^{-1}$, the surface area and porosity measured for the monolith corresponds to the catalytic layer, Table 2. The surface area of the catalytic layer and the powder catalyst are similar but a higher average pore diameter in the case of the monolith. As the pore system is the result of the interparticle void space on depositing on the alumina scale the catalyst particle packing is altered resulting in slightly higher average pore diameter.

High temperature oxidation of the metallic foil result in plate-like crystals pointing outward the metal surface of $\alpha\text{-Al}_2\text{O}_3$, which generates the typical needle-like structure usually observed upon high temperature oxidation of aluminum–alloyed ferritic stainless steels, Fig. 6 [36,39]. After washcoating a homogeneous catalytic

Table 2
Textural properties of conventional and structured catalysts.

Sample	S_{BET} ($\text{m}^2\text{ g}^{-1}$)	V_{pore} ($\text{cm}^3\text{ g}^{-1}$)	D_{pore} (Å)
Alumina powder	157	0.44	84
Catalyst powder	86	0.20	72
Alumina pellets	202	0.52	70
Catalyst pellets	123	0.34	76
Monolith	75 ^a	0.27 ^a	112

^aBET surface area of the pre-treated monolith without coating is lower than $1\text{ m}^2\text{ monolith}^{-1}$ and the values were recalculated only considering the weight of the coating and not the total weight of monolith.

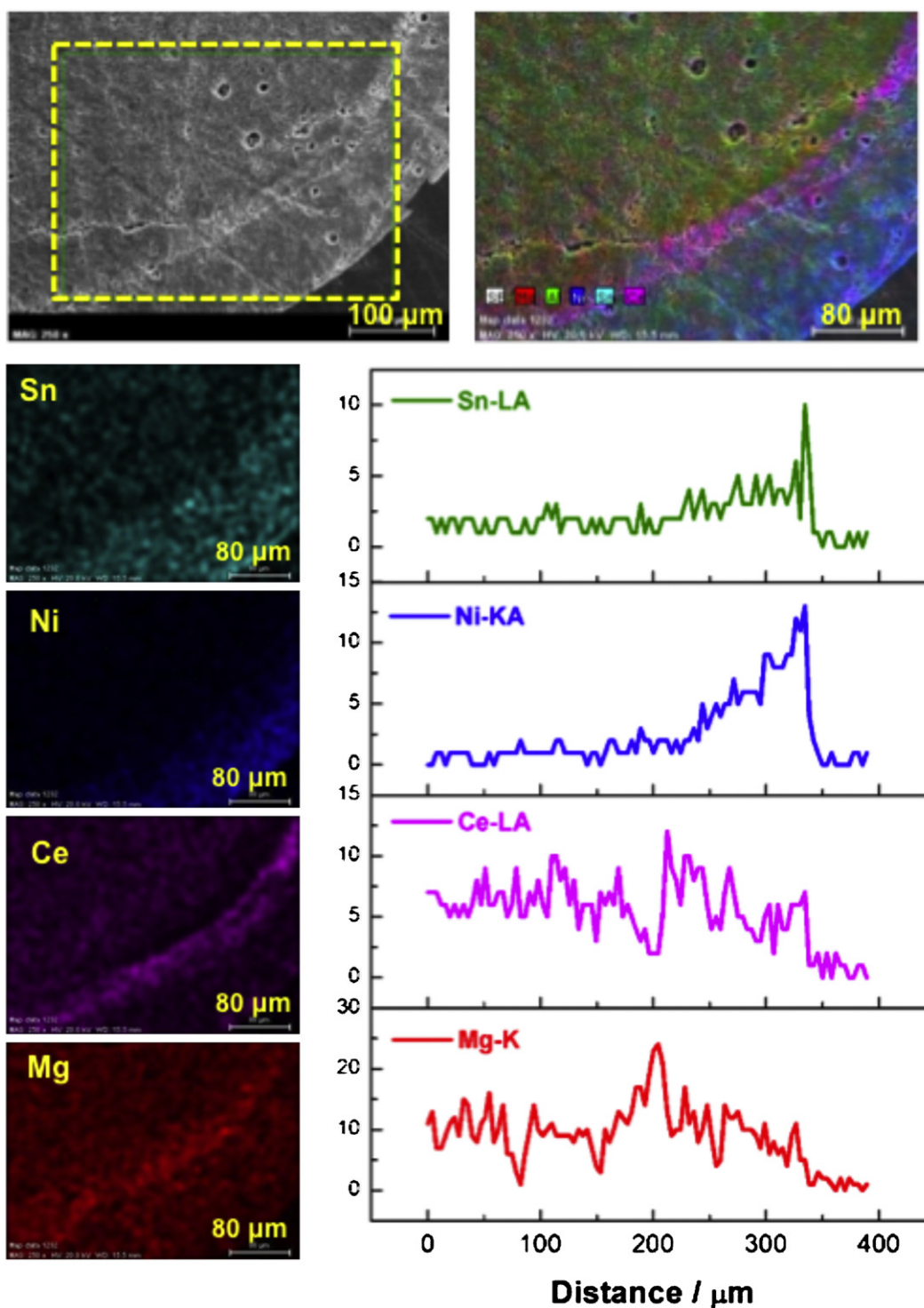


Fig. 3. SEM-EDS of the pellet cross-section.

layer is deposited showing an adherence above 95% measured through the conventional ultrasound test. A representative image is shown in Fig. 6 where cracks or spalled off areas are absent.

3.3. Catalytic activity: glycerol steam reforming

Only gas products were collected on carrying out the catalytic tests with a steam-to-carbon ratio of 4 and $100 \text{ L g}^{-1} \text{ h}^{-1}$ space velocity at 750°C . The initial hydrogen yield obtained for the prepared catalysts is hardly influenced by the catalyst morphology

being the small differences within the experimental error, Fig. 7. However, the stability is strongly dependent on the morphology. Both the powder and the pellet catalysts deactivate. In the case of the pellets the hydrogen yield drops suddenly to ca. 20% after 5 h in stream, the powders deactivation is less severe, the yield decreasing continuously reaching a value of 30% after 35 h in stream. However, the monolithic device do not deactivate at least after 55 h in the reaction stream. This rules out sintering of the active phase as responsible for the catalyst deactivation. Besides deactivation, the gas phase product distribution as a function of time on stream

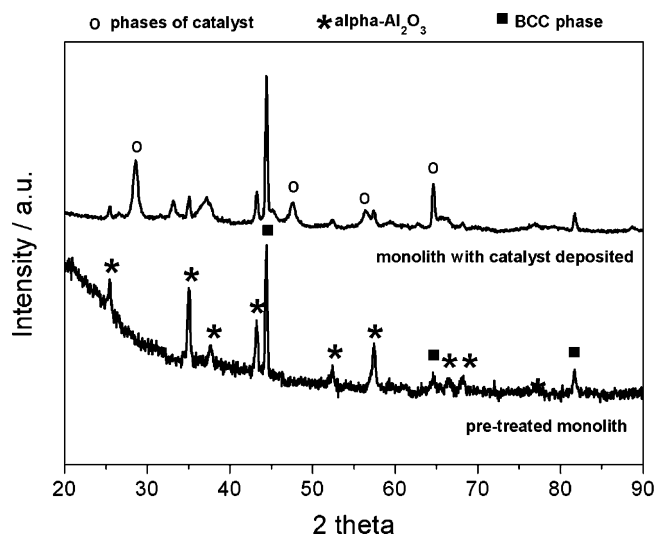


Fig. 4. XRD patterns of pre-treated monolith and monolith with catalyst deposited.

depends on the catalyst morphology, Fig. 8. The initial CO-to-CO₂ molar ratio for the three prepared catalysts is almost the same, however, for the monolithic device it remains unaltered while continuously increases in the case of the pellet and powder catalysts. This may indicate the presence of carbon deposits that may also react with the CO₂ formed according to the Boudouard reaction altering this way the CO-to-CO₂ molar ratio as the reaction proceeds and the catalyst deactivate. As both the initial hydrogen yield and the CO-to-CO₂ molar ratio are the same for the three catalysts prepared it must be concluded that the morphology and, therefore, the textural properties of the solids are responsible for the different behavior during reaction.

Valliyappan et al. [25] studied the pyrolysis of glycerol under N₂ flow at various flow rates (30–70 mL min⁻¹) and temperatures ranging from 650 to 800 °C; the obtained products were mostly gas, essentially consisting of CO, H₂, CO₂, CH₄ and C₂H₄. In their study, excellent conversion to syngas was obtained with hydrogen yields as high as 58% but this yield decreases dramatically on increasing the LHSV. On the other hand, the addition of steam enhanced the gasification of glycerol increasing the hydrogen yield by 15 mol% [26]. These authors show that the hydrogen yield depends on temperature, the nature and particle size of the packing material, the carrier flow rate and the steam-to-glycerol ratio [25,26]. However, the effect of the pyrolysis and steam gasification reaction in the absence of catalyst is absent in most of the reported studies, but investigated by Chiodo et al. [29] prior to their catalytic tests.

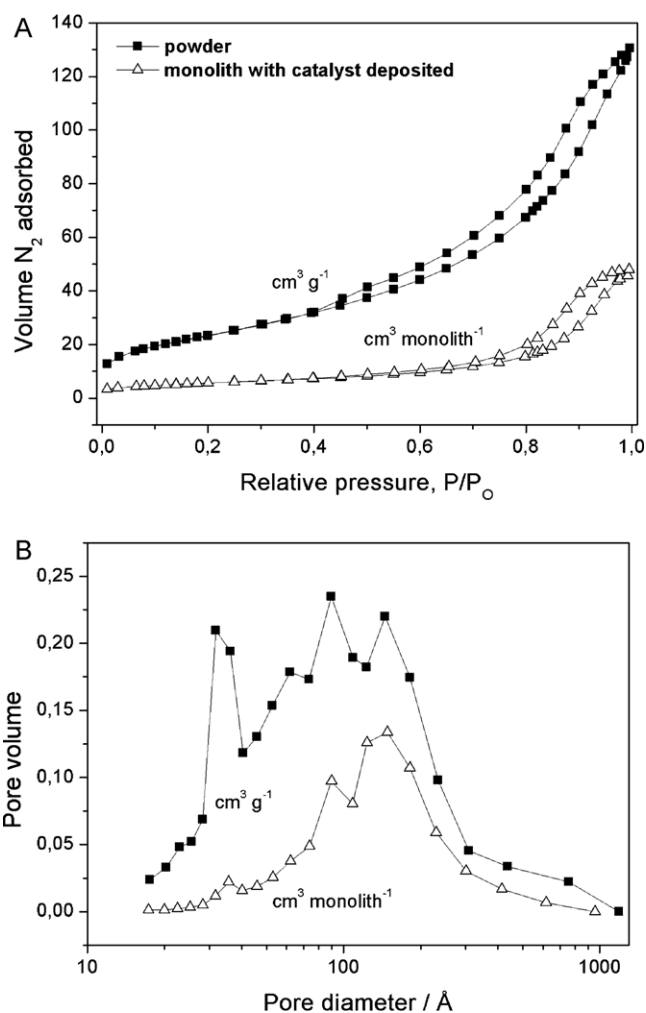


Fig. 5. Adsorption isothermal (A) and pore size distribution (B) for powder and monolith.

As glycerol is not a stable molecule at high temperature, a preliminary test without catalyst has been carried out filling the reactor with a surface pretreated metallic monolith to ascertain the extent of the pyrolysis phenomena in the SR conditions.

The glycerol conversion to gas phase products, Fig. 9, is independent of the presence of catalyst, ca. 80% conversion to gas phase products, but the hydrogen yield is well below the one obtained in the presence of the NiSn catalyst. The gas phase was essentially the same in both cases consisting of CO, H₂, CO₂, CH₄ and

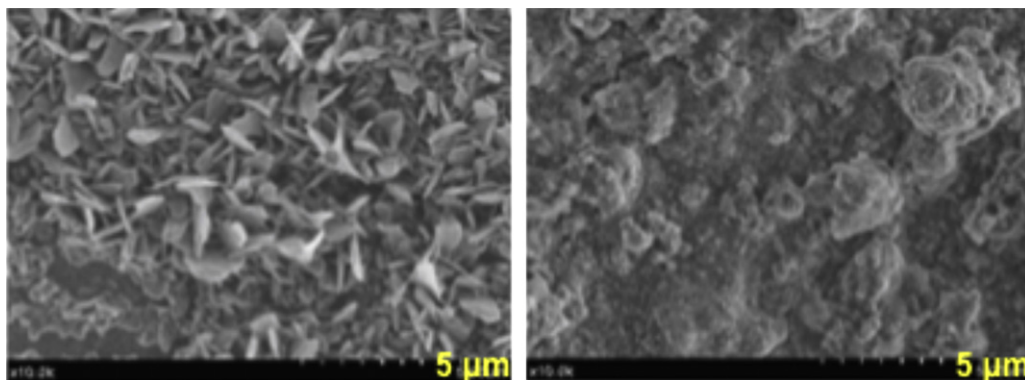


Fig. 6. SEM images of monolith pre-treated (left) and monolith with catalyst deposited (right).

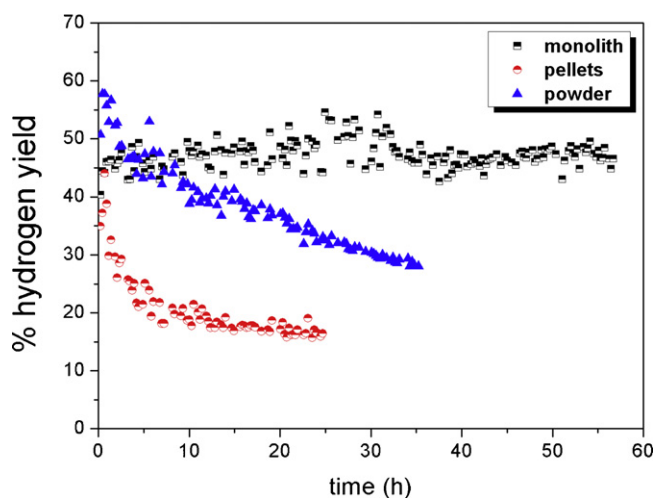


Fig. 7. Hydrogen yield in the three catalysts.

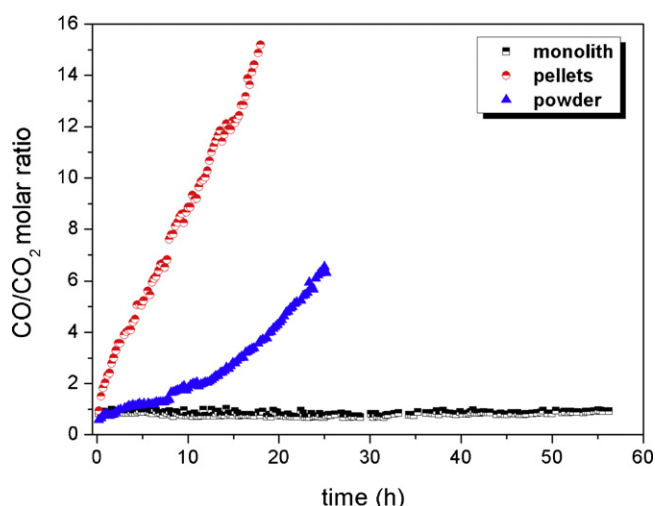
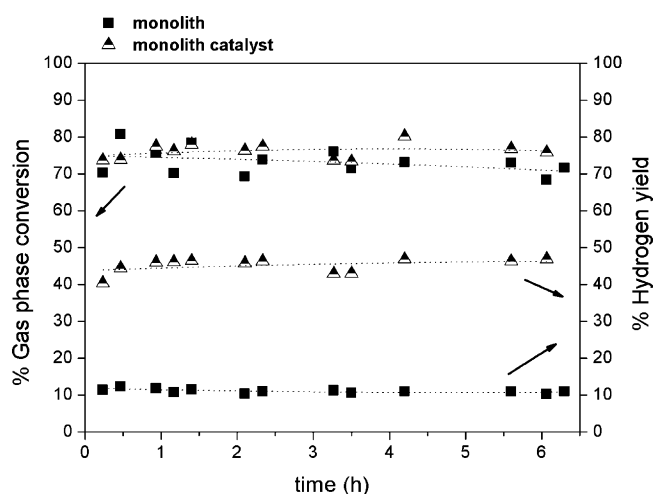
Fig. 8. CO/CO₂ molar ratio in the three catalysts.

Fig. 9. Glycerol conversion to gas products and hydrogen yield in the monolith and the monolith catalyst.

C₂H₄, but the product distribution is a function of the catalyst. Table 3 presents the gas phase product distribution for the monolith and the monolithic catalyst. The product distribution obtained in the absence of catalyst is similar to that found for the steam

Table 3

Gas phase distribution for the steam reforming of glycerol at 750 °C.

Sample	H ₂	CO	CO ₂	CH ₄	C ₂ H ₄
Monolith	28.7	45.3	1.1	13.1	10.4
Monolith catalyst	58.2	16.1	18.1	6.7	1.0
Pellets initial	59.0	16.2	17.3	6.3	1.2
Pellets final	37.1	45.0	2.7	8.7	6.5
Powder initial	58.9	12.8	21.5	6.4	0.4
Powder final	49.6	35.6	5.2	6.4	3.2

gasification of glycerol at 700 °C in a fixed-bed reactor at constant glycerol flow rate of ca. 16 cm³_{NPT} min⁻¹ using quartz chips as packing material and a molar steam-to-carbon ratios between 1 and 4 [26]. These authors reported complete conversion of glycerol to gas and char during the pyrolysis process when experiments were conducted at 700 °C. At lower temperatures and higher space velocities, Stein et al. [27] produced liquid products, mainly acrolein and acetaldehyde, in the steam gasification of glycerol in the absence of catalyst. Chiodo et al. [29] in a blank test performed at 800 °C, under SR conditions of a reaction stream containing 7% of glycerol, found that glycerol decomposes in a mixture of gaseous, 65 mol% conversion, and liquid products (ca. 30 mol% conversion), resulting in a mixture of CO (50 mol%), CO₂ (1 mol%), olefins (ethylene and propylene ca. 25 mol%), CH₄ (~13 mol%) and H₂ (~10 mol%). Although the liquid products were not properly quantified they state the presence of significant amounts of acetone, acetaldehyde, ethanol, propanol, acetic acid and 2,3-dihydroxypropional.

The observed product distributions may state that pyrolysis or pyrolysis in steam of glycerol is a complex process that includes dehydration, dehydrogenation and hydrogenolysis reactions [48]. In addition to this, the SR of these intermediate products may also take place, including steam and dry reforming of methane, particularly at temperatures above 700 °C, which may also result in carbon deposition. Therefore, under SR conditions, the steam gasification and the hydrogenation of the deposited carbon as well as the Boudouard reaction are also thermodynamically feasible.

Stein et al. [27] proposed for the pyrolysis in steam of glycerol in the 650–700 °C temperature range the decomposition in almost a equimolar mixture of acrolein (C₃H₄O) and acetaldehyde (C₂H₄O), but above 750 °C these products also decompose resulting in a mixture of carbon oxides, methane, hydrogen and ethylene by parallel bond-cleavage and radical-initiated reactions, Fig. 10. Although the glycerol conversion to gaseous products, in our case, remains constant whatever the presence or absence of catalyst the

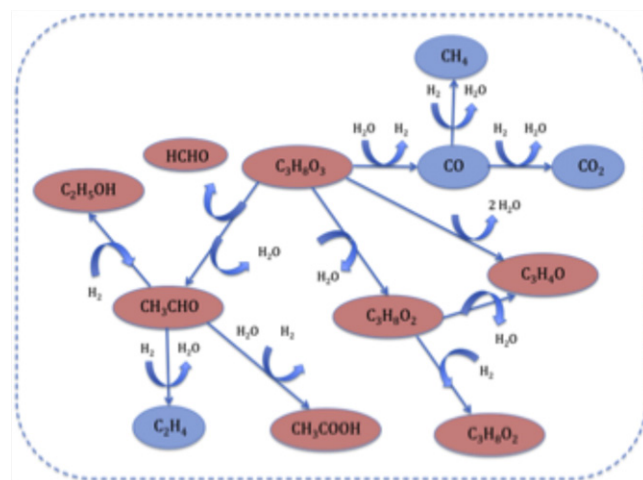
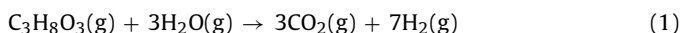


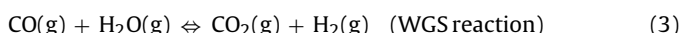
Fig. 10. Reference pathways for the steam reforming of glycerol. Adapted from reference [48].

product distribution is clearly modified. This would be associated to catalytic processes involving the glycerol decomposition products.

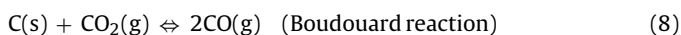
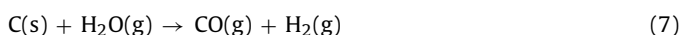
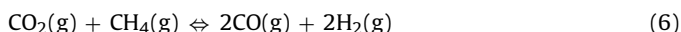
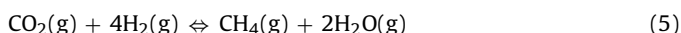
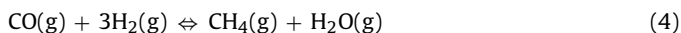
The overall reaction of hydrogen production by SR of glycerol is:



This reaction may be viewed as the combination of the glycerol decomposition and the water gas shift (WGS) reaction:



However, carbon oxides may also be consumed by the methanation reactions or produced by the steam gasification of char or the reforming of methane:



In the presence of catalyst the amount of CO, CH₄ and C₂H₄ decreases whereas the relative proportion of hydrogen and CO₂ considerably increases, Table 3. These data suggest that the CO product was most likely converted to CO₂ and H₂ via the WGS while reactions (8) and (9) are inhibited. Cheng et al. [28], in their study of glycerol SR over bimetallic Co–Ni catalysts, conclude that carbon deposition during reaction is responsible for the loss in surface area and pore volume of the used catalysts. The steam gasification of these carbon deposits together with the WGS reaction may also account for the increased proportion of H₂ and CO₂ observed on the monolithic catalyst, Table 3. This carbon gasification reaction competes with the Boudouard reaction as well as carbon hydrogenation reducing the relative proportion of methane and CO present in the reaction products. Araque et al. [30] found, for the glycerol SR over CeZrCo oxides, a similar trend on deactivating their catalyst, the H₂ and CO₂ production decrease while the production of CO, CH₄ and C₂H₄ increases. For these authors methane formation proceeds through carbon monoxide methanation while ethylene would be produced by hydrogenation/dehydration of acetaldehyde according to the scheme in Fig. 10. Kinetic data for CoNi/Al₂O₃ catalysts suggest, however, that CH₄ is originated from the hydrogenolysis of glycerol ruling out the methanation reaction as a path for methane production [28].

The initial gas product distribution for the powder and pellet catalysts follows the same trend observed for monolithic catalyst but this distribution changes as catalysts deactivate, Table 3, approaching the values observed for the steam gasification of glycerol in the absence of catalyst [25–27,29]. This indicates that only the thermal pyrolysis in steam of glycerol operates after catalyst deactivation.

3.4. Post-reaction analysis

The existence of carbon deposits on the catalyst surface is analyzed by combining TPD and TPO experiments. TPD data (not shown) indicate only water desorption, which discards the presence of adsorbed carbon oxides and/or oxygenated carbon species that may result in carbon oxides upon heating. TPO data show, however, evolution of CO₂. Fig. 11 presents the evolution of the *m/z* = 44 (CO₂) signal in the TPO experiments. The catalysts in the form of powders and pellets present an intense peak at 730 and 750 °C, respectively, confirming the existence of highly structured carbon deposits, however the monolithic device shows a weak signal at

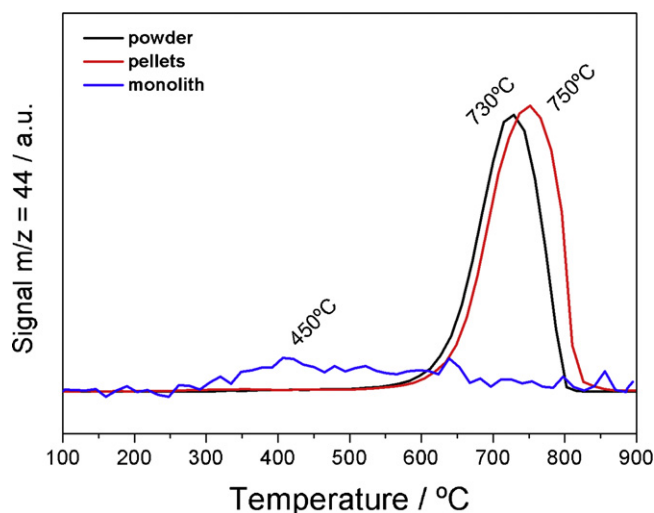


Fig. 11. TPO profile after reaction in the three catalysts.

450 °C indicating that the elimination of carbon deposits is easier. As the area under the TPO curve is proportional to the amount of deposited carbon it must be stated that for the monolithic device carbon deposition is unimportant, which is in accordance with the observed stability for this catalyst.

In their study on coke deposition over Pt/CeO₂–ZrO₂ catalysts, Noronha et al. [49] indicate that carbon oxidation is catalyzed by the metal particles at the metal–support interface. The peak at lower temperatures might be assigned to carbon near metallic particles or to amorphous carbon and the peak at higher temperature to graphitic carbon over the support [49,50]. TPR–TPO experiments performed on reacted Co–Ni catalysts revealed at least two types of carbonaceous deposits, one of these carbon pools resistant to removal with H₂ [28].

The different nature of the carbon deposits as a function of the catalyst shape cannot be related to the existence of different surface sites since all the catalysts have the same composition and the initial catalytic activity and selectivity are similar. The textural properties of the deactivated catalysts may throw some light on the deactivation process. The pore volume and specific surface area of the deactivated catalysts are shown in Table 4. After reaction pore volume and specific surface area for all the catalysts except the monolithic one decrease pointing to a deactivation process by a pore blocking mechanism by deposited carbon, a similar mechanism has been proposed for the catalyst deactivation by Cheng et al. [28]. On the contrary, the monolithic catalyst keeps its textural properties after 55 h under reaction (Fig. 12) ruling out that the textural modification, upon reaction, were due to the sealing of alumina pore mouth in the presence of steam.

Raman spectroscopy is a standard tool for the characterization of carbons with different degrees of graphitic ordering and, therefore, it has been used for characterizing the structure of coke deposits.

Table 4
Textural properties before and after reaction.

Sample	<i>S</i> _{BET} (m ² g ^{−1})	<i>V</i> _{pore} (cm ³ g ^{−1})	<i>D</i> _{pore} (Å)
Monolith	75 ^a	0.27 ^a	112
Monolith after reaction	76 ^a	0.30 ^a	119
Powder	86	0.20	72
Powder after reaction	63	0.15	84
Pellets	123	0.34	76
Pellets after reaction	57	0.17	94

^aBET surface area of the pre-treated monolith without coating is lower than 1 m² monolith^{−1} and the values were recalculated only considering the weight of the coating and not the total weight of monolith.

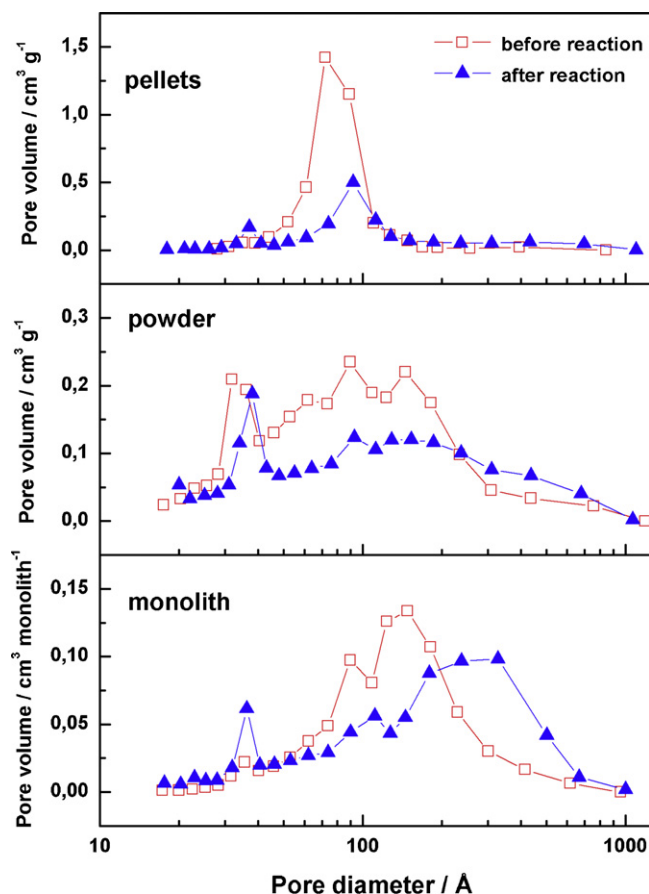


Fig. 12. Pore size distribution for the catalysts after reaction.

Fig. 13 shows the Raman spectra of three catalysts after reaction. The first-order Raman spectra of all the samples is characterized by two sharp peaks with maxima at ca. 1590 and 1345 cm^{-1} , which are typical of sp^2 -bonded carbon. The Raman spectra of disordered graphite show two modes, the G peak around 1580–1600 cm^{-1} and the D peak around 1350 cm^{-1} , usually assigned to phonons of E_{2g} and A_{1g} symmetry, respectively [51]. However, whatever the graphitic ordering the G and D peaks dominate the Raman spectra of sp^2 -bonded carbons, but the intensity, position, and width of these peaks allow the structural characterization of the deposited coke. According to Ferrari and Robertson [52] on going from nanocrystalline graphite to amorphous carbon the position of the G band shifts downward while the D-to-G intensity ratio decreases. The frequency of the A_{1g} mode follows the sequence:

Pellet > Powder > Monolith

This sequence indicates the graphitic ordering of the carbon deposits and is similar to the temperature at which the TPO peak appears, Fig. 11.

In general it is assumed that on decreasing the D-to-G intensity ratio the degree of graphitization increases [53,54]. The D-to-G intensity ratio for the three catalysts is:

Pellet(1.16) < Powder(1.22) < Monolith(1.32)

Therefore, the monolithic catalyst presents the lowest graphitic ordering as the TPO data suggest.

SEM data, Fig. 14, confirm the differences in graphitic ordering of the coke deposits. Fig. 14 shows the cross section of a pellet after reaction. The cross-section of a pellet after reaction is coated by a thick carbon layer in which the presence of carbon nanofibers

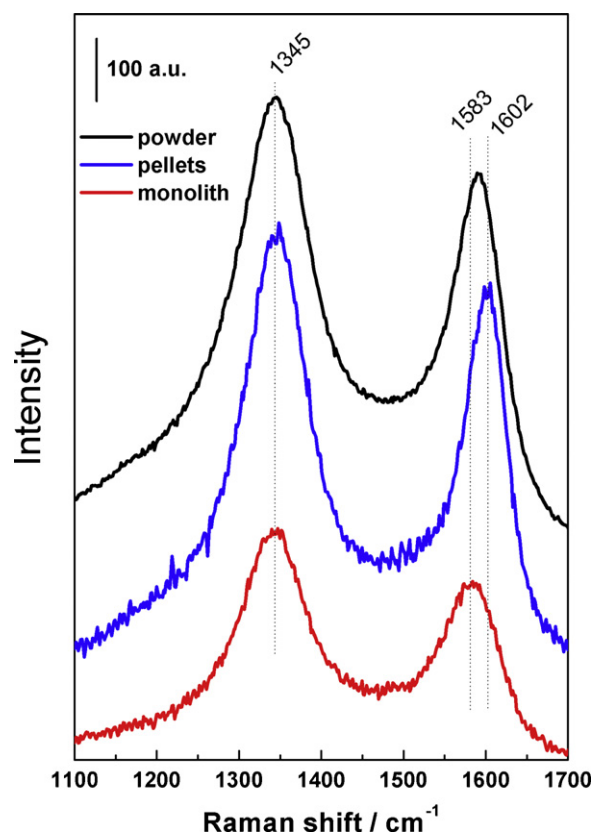


Fig. 13. Raman spectra of catalysts after reaction.

is noticed, Fig. 14. In the powder catalyst the morphology and textural characteristics are lost and just carbon fibers are observed indicating that all the particles area surrounded by carbon. For the monolithic catalyst carbon is not observed and the morphological and textural properties remains unaltered.

3.5. Scheme of a model

A scheme of a model for explaining the obtained results is shown in Fig. 15. The catalyst particle size is critical in this scheme since it alters the surface-to-volume (S/V) ratio of the catalysts. The pellets have 1.8 mm average diameter, the powder catalyst was sieved to particle sizes between 100 and 200 μm , while assuming the metallic surface area, the catalyst loading and the solid theoretical density the thickness of the washcoated layer is estimated in 4.2 μm . These result in S/V ratios of ca. 3, 40 and 250 mm^{-1} for pellet, powder and monolithic catalysts, respectively. Therefore, if carbon blocking of active sites is responsible for catalyst deactivation, on decreasing the S/V ratio an enhancement of the deactivation process should be expected. For the high temperature steam gasification of glycerol an increase of the S/V ratio, from 2 to 30 mm^{-1} , results in an increase in the yield of gaseous products and char with simultaneous decrease in yield of liquid products whatever the packing material used for the reactor [25]. This behavior is explained on the basis of an enhancement of plug flow behavior as well as heat transfer in the reactor that increases liquid conversion to gas and char. However, our results indicate that on increasing the S/V ratio the amount of deposited char decreases, particularly for the catalyst deposited in the microchannel device where plug flow behavior is expected.

The sequential reaction scheme in which glycerol is converted into liquid products and these further reformed to carbon oxides and hydrogen is clear by modifying the glycerol residence time in

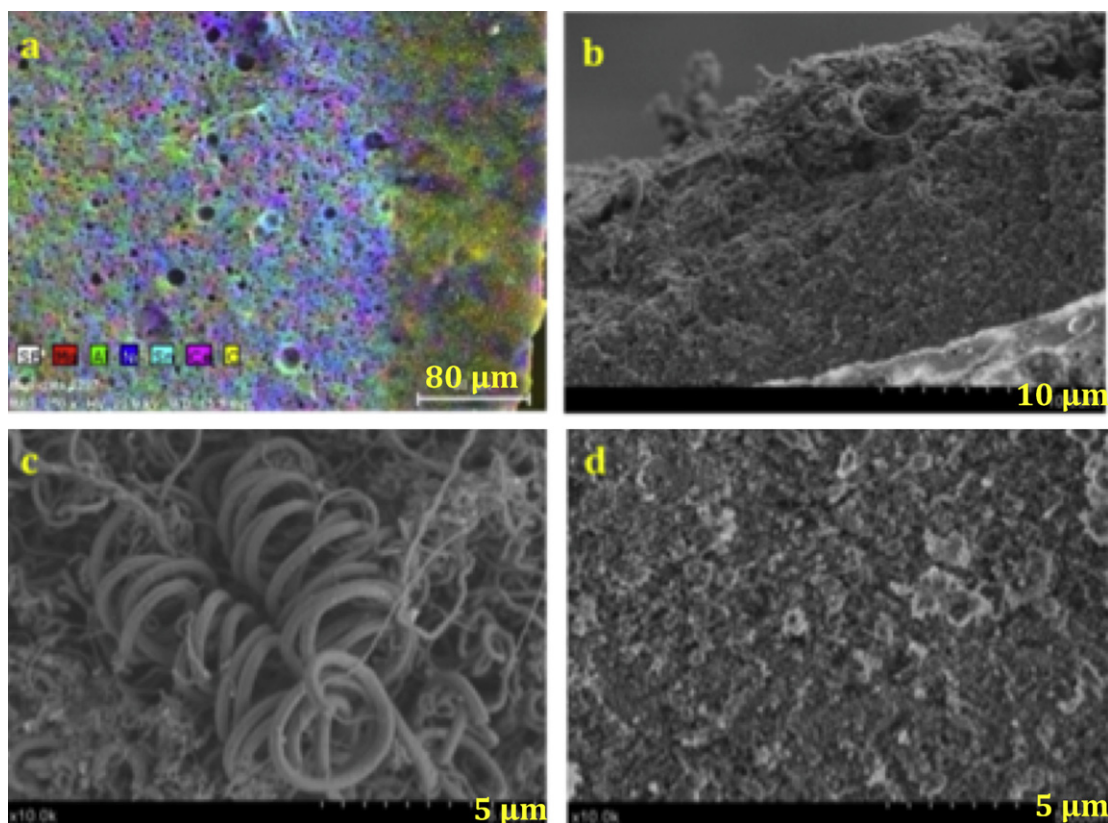


Fig. 14. SEM images of catalysts after reaction: EDS (A) and SEM (B) of pellets cross-section, powder (C) and monolith (D).

the reactor. As the residence time increase liquids are converted to gaseous products in the presence of steam, Fig. 16. The product distribution of liquids, Fig. 17, accounts for the presence of acid and basic sites showing the presence of dehydration products as hydroxyacetone, the main liquid product whatever the residence time (~40%), and dehydrogenation by-products as glyceraldehyde (~20%), further reaction sequences account for the presence of 1,2- and 1,3-propanediol, acroleyn, acetone, propanal, methanol, ethanol, 2-propanol, formic, acetic and lactic acids depending their

concentrations on the residence time [55]. This product distribution agrees fairly well with the sequential reaction scheme for glycerol decomposition [48,56]. In these schemes the formation of glycerol oligomers resulting in coking reaction [57] and coke formation from ethylene, acrolein or acetaldehyde is considered [56,58], and probably acroleyn; coke can be formed from many sources.

Therefore, on increasing the S/V ratio and the residence time the formation of coke should be favored. However, in a simplified scheme the net coke formation is the result of the carbon formation

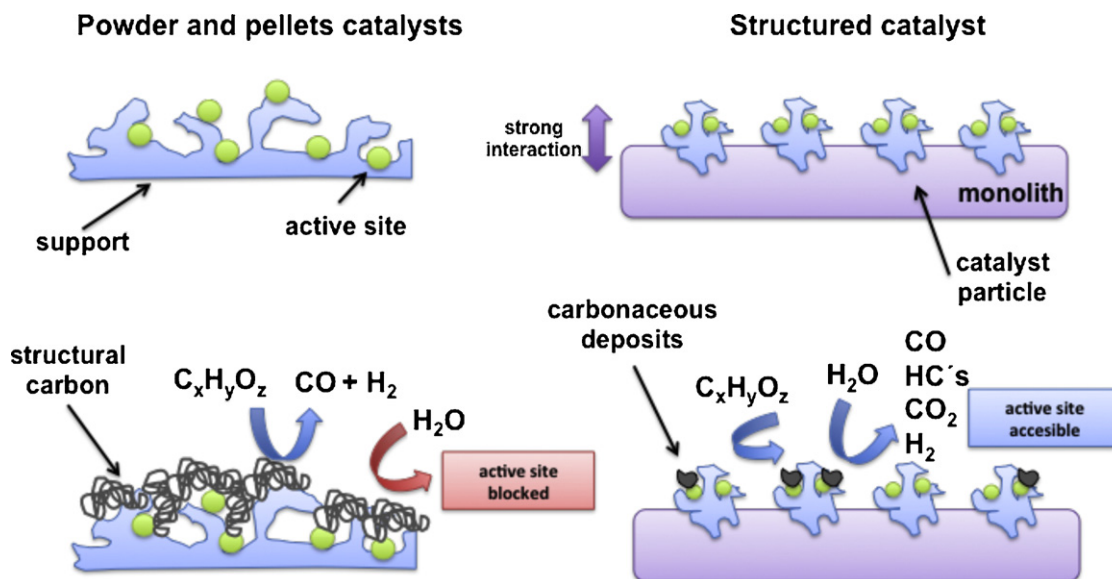


Fig. 15. Schematic representation of reaction in the studied systems.

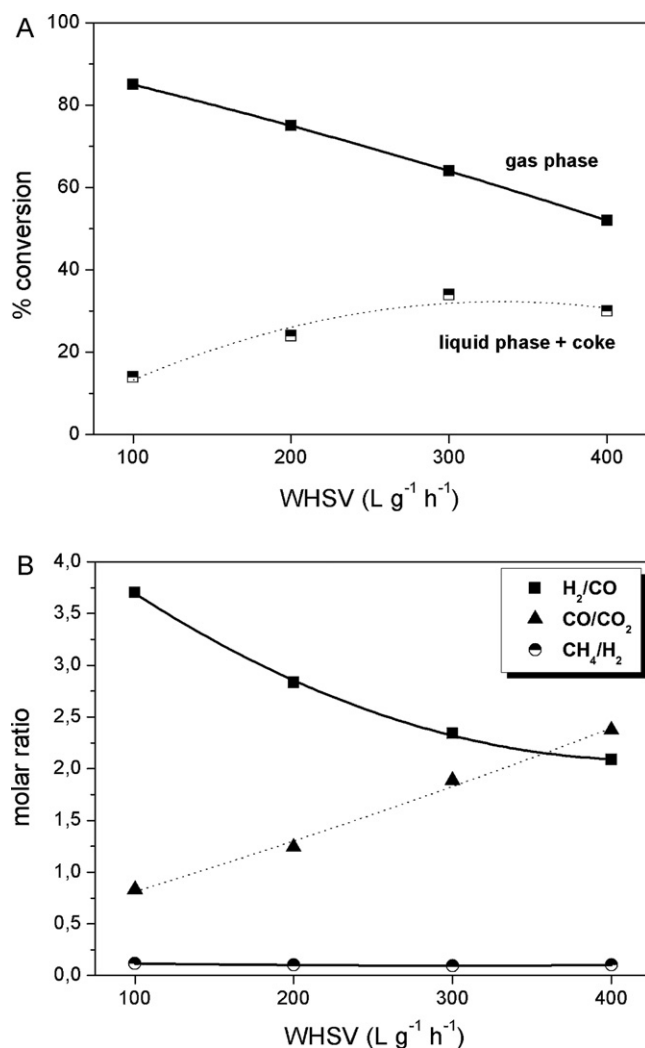


Fig. 16. Glycerol conversion (A) and molar ratio H₂/CO, CO/CO₂ and CH₄/H₂ (B) over the monolithic catalyst as a function of WHSV. Data plotted corresponds to reaction products after 2 h.

and carbon gasification kinetics, reactions (10) and (11) [59], and obviously the increase in the S/V ratio also increases the rate of carbon gasification enhancing the catalyst stability.



The decrease of the S/V ratio favors the coking reaction with respect to the gasification reaction resulting in pore blocking and loss of active sites deactivating the catalyst. In addition to this, coke grows in the interparticle space blocking the reaction path for the powder and the pellet catalysts, the strong interaction between the catalyst particles and the alumina layer grown on the monolith metallic surface prevents the interaction between the catalyst particles.

The catalyst morphology alters the catalyst effectiveness that has a strong influence in the reforming process [60], the higher the S/V ratio the higher the carbon formation rate but, at the same time, as carbon may be gasified by water in the presence of Ni catalysts [61–63] the higher the rate of carbon gasification and the lower the amount of carbon remaining in the catalyst surface and therefore the deactivation process.

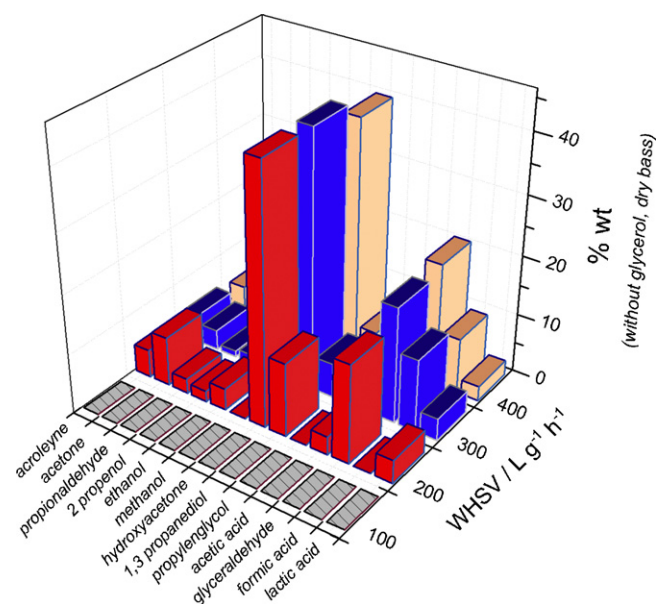


Fig. 17. Effect of WHSV in the liquid production over the monolithic catalyst. Data estimated after 2 h of reaction.

4. Conclusions

A structured catalyst (monolith) and conventional catalysts (spherical pellets and powder) have been compared in the glycerol steam reforming. All catalysts showed the same activity and selectivity for the first hour, but the conventional catalysts were rapidly deactivated. The structured catalyst was not deactivated after 50 h of reaction. TPO profile showed that coke formation is minimized in the monolith and the textural properties reveal that in conventional catalyst is deposited in the pores blocking all the active sites. Besides, Raman results reveals that the monolithic catalyst presents the lowest graphitic ordering as the TPO data suggest. Coke formation was not observed in the monolith catalyst owed to the strong interaction between the catalyst particles and the alumina layer in the monolith.

Acknowledgements

L.F. Bobadilla and A. Álvarez also thanks the “Junta de Andalucía” for their research fellowships associated to PO6-TEP01965 and PO9-TEP-5454, respectively. Financial support for this work has been obtained from the Spanish “Ministerio de Ciencia e Innovación” (ENE2009-14522-C05-01) and from “Junta de Andalucía” (POG-TEP01965). Both contracts are cofunded by FEDER funds from the European Union.

References

- [1] Y. Wang, K.S. Chen, J. Mishler, S.C. Cho, X.C. Adroher, *Applied Energy* 88 (2011) 981.
- [2] C.C.R.S. Rossi, C.G. Alonso, O.A.C. Antunes, R. Guirardello, L. Cardozo-Filho, *International Journal of Hydrogen Energy* 34 (2009) 323.
- [3] T. Abbasi, S.A. Abbasi, *Renewable and Sustainable Energy Reviews* 15 (2011) 3034.
- [4] J. Barton, R. Gammon, *Journal of Power Sources* 195 (2010) 8222.
- [5] R. Kleijn, E. van der Voet, *Renewable and Sustainable Energy Reviews* 14 (2010) 2784.
- [6] D.B. Levin, R. Chahine, *International Journal of Hydrogen Energy* 35 (2010) 4962.
- [7] M.A.K. Lodhi, *International Journal of Hydrogen Energy* 12 (1987) 461.
- [8] P. Moriarty, D. Honnery, *International Journal of Hydrogen Energy* 32 (2007) 1616.
- [9] V. Subramani, C. Song, M. Anpo, J.M. Andresen, *Catalysis Today* 129 (2007) 263.
- [10] S. Adhikari, S.D. Fernando, A. Haryanto, *Renewable Energy* 33 (2008) 1097.
- [11] T. Hirai, N.-o. Ikenaga, T. Miyake, T. Suzuki, *Energy & Fuels* 19 (2005) 1761.

- [12] I.N. Buffoni, F. Pompeo, G.F. Santori, N.N. Nichio, *Catalysis Communications* 10 (2009) 1656.
- [13] R.D. Cortright, R.R. Davda, J.A. Dumesic, *Nature* 418 (2002) 964.
- [14] D.L. Trimm, *Catalysis Today* 49 (1999) 3.
- [15] J.W. Shabaker, D.A. Simonetti, R.D. Cortright, J.A. Dumesic, *Journal of Catalysis* 231 (2005) 67.
- [16] A. Penkova, L. Bobadilla, S. Ivanova, M.I. Domínguez, F. Romero-Sarria, A.C. Roger, M.A. Centeno, J.A. Odriozola, *Applied Catalysis A: General* 392 (2011) 184.
- [17] L.F. Bobadilla, C. García, J.J. Delgado, O. Sanz, F. Romero-Sarria, M.A. Centeno, J.A. Odriozola, *Journal of Magnetism and Magnetic Materials*, under review.
- [18] Z.L. Zhang, X.E. Verykios, *Catalysis Today* 21 (1994) 589.
- [19] O. Yamazaki, T. Nozaki, K. Omata, K. Fujimoto, *Chemistry Letters* 21 (1992) 1953.
- [20] K. Tomishige, Y.g. Chen, K. Fujimoto, *Journal of Catalysis* 181 (1999) 91.
- [21] D. Hufschmidt, L.F. Bobadilla, F. Romero-Sarria, M.A. Centeno, J.A. Odriozola, M. Montes, E. Falabella, *Catalysis Today* 149 (2010) 394.
- [22] D.L. Trimm, Z.I. Önsan, *Catalysis Reviews: Science and Engineering* 43 (2001) 31.
- [23] V. Meeyoo, J.H. Lee, D.L. Trimm, N.W. Cant, *Catalysis Today* 44 (1998) 67.
- [24] V.A. Tsipouriari, Z. Zhang, X.E. Verykios, *Journal of Catalysis* 179 (1998) 283.
- [25] T. Valliyappan, N.N. Bakhshi, A.K. Dalai, *Bioresource Technology* 99 (2008) 4476.
- [26] T. Valliyappan, D. Ferdous, N. Bakhshi, A. Dalai, *Topics in Catalysis* 49 (2008) 59.
- [27] Y.S. Stein, M.J. Antal Jr., M. Jones Jr., *Journal of Analytical and Applied Pyrolysis* 4 (1983) 283.
- [28] C.K. Cheng, S.Y. Foo, A.A. Adesina, *Industrial & Engineering Chemistry Research* 49 (2010) 10804.
- [29] V. Chiodo, S. Freni, A. Galvagno, N. Mondello, F. Frusteri, *Applied Catalysis A: General* 381 (2010) 1.
- [30] M. Araque, L.M.T. Martínez, J.C. Vargas, A.C. Roger, *Catalysis Today* 176 (2011) 352.
- [31] J. Li, H. Yu, G. Yang, F. Peng, D. Xie, H. Wang, J. Yang, *Energy & Fuels* 25 (2011) 2643.
- [32] C.D. Dave, K.K. Pant, *Renewable Energy* 36 (2011) 3195.
- [33] G. Yang, H. Yu, F. Peng, H. Wang, J. Yang, D. Xie, *Renewable Energy* 36 (2011) 2120.
- [34] G. Arzamendi, P.M. Diéguez, M. Montes, J.A. Odriozola, E. Falabella Sousa-Aguar, L.M. Gandía, *Chemical Engineering Journal* 160 (2010) 915.
- [35] G. Arzamendi, P.M. Diéguez, M. Montes, J.A. Odriozola, E.F. Sousa-Aguar, L.M. Gandía, *Chemical Engineering Journal* 154 (2009) 168.
- [36] D.M. Frías, S. Nouisir, I. Barrio, M. Montes, L.M.T. Martínez, M.A. Centeno, J.A. Odriozola, *Applied Catalysis A: General* 325 (2007) 205.
- [37] L.M.T. Martínez, D.M. Frías, M.A. Centeno, A. Paúl, M. Montes, J.A. Odriozola, *Chemical Engineering Journal* 136 (2008) 390.
- [38] O. Sanz, L.C. Almeida, J.M. Zamaro, M.A. Ulla, E.E. Miró, M. Montes, *Applied Catalysis B: Environmental* 78 (2008) 166.
- [39] L.C. Almeida, O. González, O. Sanz, A. Paul, M.A. Centeno, J.A. Odriozola, M. Montes, *Studies in Surface Science and Catalysis Volume* 167 (2007) 79.
- [40] L.C. Almeida, F.J. Echave, O. Sanz, M.A. Centeno, G. Arzamendi, L.M. Gandía, E.F. Sousa-Aguar, J.A. Odriozola, M. Montes, *Chemical Engineering Journal* 167 (2011) 536.
- [41] S. Vallar, D. Houivet, J. El Fallah, D. Kervadec, J.M. Haussonne, *Journal of the European Ceramic Society* 19 (1999) 1017.
- [42] L.C. Almeida, F.J. Echave, O. Sanz, M.A. Centeno, J.A. Odriozola, M. Montes, *Studies in Surface Science and Catalysis* 175 (2010) 25.
- [43] T.A. Nijhuis, A.E.W. Beers, T. Vergunst, I. Hoek, F. Kapteijn, J.A. Moulijn, *Catalysis Reviews* 43 (2001) 345.
- [44] Y.Y.S. Yasaki, K. Ohkubo, US Patent 5 208 206 (1993).
- [45] F. Aupretre, C. Descorme, D. Duprez, D. Casanave, D. Uzio, *Journal of Catalysis* 233 (2005) 464.
- [46] L.M.T. Martínez, M.I. Domínguez, N. Sanabria, W.Y. Hernández, S. Moreno, R. Molina, J.A. Odriozola, M.A. Centeno, *Applied Catalysis A: General* 364 (2009) 166.
- [47] L.M. Martínez T, PhD Thesis, Universidad de Sevilla (2008).
- [48] S. Adhikari, S.D. Fernando, A. Haryanto, *Energy Conversion and Management* 50 (2009) 2600.
- [49] F.B. Noronha, E.C. Fendley, R.R. Soares, W.E. Alvarez, D.E. Resasco, *Chemical Engineering Journal* 82 (2001) 21.
- [50] R. Baccud, H. Charcosset, M. Guenin, R. Torrellas-Hidalgo, L. Tournayan, *Applied Catalysis* 1 (1981) 81.
- [51] M.S. Dresselhaus, G. Dresselhaus, A. Jorio, A.G. Souza Filho, R. Saito, *Carbon* 40 (2002) 2043.
- [52] A.C. Ferrari, J. Robertson, *Physical Review B* 61 (2000) 14095.
- [53] S. Gil, L. Muñoz, L. Sánchez-Silva, A. Romero, J.L. Valverde, *Chemical Engineering Journal* 172 (2011) 418.
- [54] A. Nieto-Márquez, S. Gil, A. Romero, J.L. Valverde, S. Gómez-Quero, M.A. Keane, *Applied Catalysis A: General* 363 (2009) 188.
- [55] L.F. Bobadilla, PhD Thesis, Universidad de Sevilla (2011).
- [56] A. Corma, G.W. Huber, L. Sauvanaud, P. O'Connor, *Journal of Catalysis* 257 (2008) 163.
- [57] J. Barrault, J.M. Clacens, Y. Pouilloux, *Topics in Catalysis* 27 (2004) 137.
- [58] A.G. Gayubo, A.T. Aguayo, A. Atutxa, R. Aguado, J. Bilbao, *Industrial & Engineering Chemistry Research* 43 (2004) 2610.
- [59] J.R. Rostrup-Nielsen, J. Sehested, *Studies in Surface Science and Catalysis* 139 (2001) 1.
- [60] L.J.C.J.R. Rostrup-Nielsen, *Concepts in Syngas Manufacture*, Imperial College Press, London, 2011.
- [61] C.R.F. Lund, *Carbon* 25 (1987) 337.
- [62] Y. Nishiyama, T. Haga, O. Tamura, N. Sonehara, *Carbon* 28 (1990) 185.
- [63] K.S. Colle, K. Kim, A. Wold, *Fuel* 62 (1983) 155.